JACS Au
AN OPEN ACCESS JOURNAL OF THE AMERICAN CHEMICAL SOCIETY

pubs.acs.org/jacsau
Article

Tracking of Active Sites as Well as the Compositing Effect over a Cu/Ce-Based Catalyst with Superior Catalytic Activity

Jin Zhang, Hongyu Lin, Xiaoqin Zhang, Mingli Fu, and Daiqi Ye*

Cite This: JACS Au 2025, 5, 975−989
Read Online

ACCESS | Metrics & More | Article Recommendations | Supporting Information

ABSTRACT: The replacement of a noble metal catalyst by base metals presents a great challenge for low-temperature CO and volatile organic compounds oxidation. Cu/Ce-based catalysts are expected to achieve this goal with excellent performance, among which the main active sites still need to be further explored. For this reason, CuCe catalysts were further compounded with typical elements (cobalt, Co) to study the main active sites and compositing effect by in-situ enhanced Raman and in-situ ultralow-temperature DRIFTS technologies. The main active site for both CuCe and CuCoCe catalysts was the same Cu−O_V−Ce at the copper−cerium interface, named as asymmetric oxygen vacancy (ASOv). The dispersion of CuO and CeO_2 species was promoted, and the formation energy of ASOv was decreased significantly from 1.502 to 0.854 eV after the addition of Co, which leads to an increase in the ASOv concentration. A small cobalt added can form more Co^{2+} species, improving the activity and stability. The activity of $Cu_1Co_{0.5}Ce_3$ catalyst was significantly improved with 100% conversion of CO and toluene at 96 and 227 °C. Here, the ASOv was studied in relative quantification, showing consistency of catalytic activity and ASOv concentration. Meanwhile, the dynamic exchange of ASOv in the reactions was tracked, indicating that the redox equilibrium of ASOv can continuously produce new ASO_V in Cu/Ce-based catalysts that cause long-term catalytic stability. In addition, it is almost difficult for CoCe and CoCu samples to form the ASOv, and the interaction between metals and metals was also weaker than that of CuCe and CuCoCe catalysts.

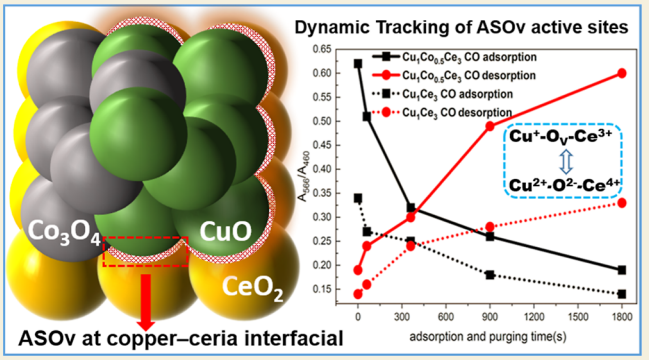

KEYWORDS: *Copper−cobalt-ceria catalysts, asymmetric oxygen vacancy, active sites, CO and VOCs oxidation, in-situ enhanced techniques*

1. INTRODUCTION

The rapid expansion of global modernization and industrialization has made the atmospheric environment on which human beings depend increasingly polluted.[1−3] Volatile organic compounds (VOCs) and carbon monoxide (CO) in typical atmospheric pollutants were abundant in industrial and automobile exhaust, which are extremely harmful to humans and the environment.[4−6] The removal of VOCs and CO was currently mainly catalytic degradation technology, and catalysts were the core components.[7,8] The widely used noble metal catalyst is scarce, expensive, and sensitive to CO and CO_2 poisoning, which seriously hinders the development of catalytic degradation technology for atmospheric pollution control; hence, it is urgent to research high-performance non-noble metals catalysts to replace it.[9−11]

Copper−cerium non-noble metal catalysts has the great potential in air pollution treatment, and it shows the performance advantages in CO oxidation, VOCs oxidation, preferential oxidation of CO in excess hydrogen, water−gas conversion, CO/CO_2 hydrogenation, NOx reduction, and other reactions.[12−20] It is mainly due to the strong metal−support interaction, promoting the unique Cu−Ox−Ce active species generated at the interface between Cu and Ce in copper−cerium composite oxides. The active site of Cu−Ce catalysts was usually similar to that of noble metal Ce-based catalysts (Pd/CeO_2, Au/CeO_2 and Pt/CeO_2), and that the key to catalytic activity was the dispersion of Cu, Pd, Au, and Pt on the CeO_2 surface.[21−23] Therefore, the activity of CuO/CeO_2 mainly depends on the fact that highly dispersed CuO can produce a large number of interfaces between copper and cerium dioxide, contributing more Cu−Ox−Ce species.[24−26] CeO_2 is often considered as a donor of reactive oxygen species in REDOX reactions, contributing a large number of oxygen vacancies because of unique fluorite type structure contributed.[27] Many studies have shown that oxygen vacancies act as

Received: December 15, 2024
Revised: January 15, 2025
Accepted: January 20, 2025
Published: January 29, 2025

active sites in most catalytic oxidation reactions.[28,29] However, the oxygen vacancy (O_V) of $Ce^{3+}-O_V-Ce^{4+}$ species contained in pure CeO_2 is a symmetrical coordination structure limiting the rate of electron transfer and resulting in a slower formation rate of active oxygen on pure CeO_2 than on binary or ternary Ce-based catalysts.[30] In recent years, more and more attention has been paid to Ce-base catalysts, especially the study of promoting electron transport in the asymmetric coordination environment of Ov.[31,32] The symmetry of Ov in composite oxides formed by transition metal especially CuO and CeO_2 has become the focus of research.[33,34] The study showed that binary metal oxides can form asymmetric Ov in an asymmetric coordination environment; however, there was a lack of in-depth research and effective experimental demonstration of only the prediction and theoretical calculation.

It is a long-term goal to improve the low-temperature activity and stability of Cu−Ce catalysts to achieve replacement of the noble metal catalyst. Studies have been conducted to catalytic degradation of typical atmospheric pollutants by combining third element (such as iron, nickel and Indium) in the Cu−Ce catalysts.[9,19,35] However, the addition of these elements does not significantly improve the performance of Cu−Ce based catalysts except for cobalt. Copper−cobalt−cerium (CuCoCe) ternary catalysts prepared by different methods have been studied for the catalytic oxidation of CO and VOCs, showing a better performance.[36−49] Different morphologies have a great influence on the activity, in fact, because the morphologies change the concentration of the exposed active site on the catalyst surface, showing the difference of activity. The diverse interface and core−shell structures have be designed and synthesized, indicating the dispersity of surface CuO species was enhanced due to stronger interaction, which enhance oxidation activities and durability.[36,49] The influence of calcination temperature and sedimentation pH on the structure and activity of CuCoCe catalysts has also been studied for CO oxidation, and results show that both they play a crucial role in determining the physicochemical properties such as surface area, particle sizes, and valence states of the elements on the surface of the catalysts. Further studies showed that the Cu^+ were relatively enriched on the surface of CuCoCe, and the synergistic effect by ternary mixed oxide and the oxidability-reducibility between Cu^{2+} to Cu^+ was the important factor for performance.[43,46] However, there is a lack of in-depth insight into the active sites of the CuCoCe catalysts. The study showed that O_2 in the gas phase was dissociated into atomic oxygen and was adsorbed in the vacancy at the Co−Ce interface with further diffusion into the CO−Cu^+ site achieving oxidation of CO.[45] There is more evidence that Cu ion plays a major role in the CuCoCe catalyst, while the coordination structure of Cu^+ active site and the role of cobalt in it are still uncertain. In Cu−Ce catalysts, the main active site was asymmetric oxygen vacancy (ASOv), and the coordination structure is an active center composed of copper, cerium, and connected oxygen vacancies.[50,51] Whether ASOv can be formed steadily in ternary CuCoCe catalysts, what is the main active site, and the effect of cobalt recombination in Cu−Ce-based catalysts all these need to be further explored.

The active sites of CuCe catalysts for CO and toluene have been explored in our earlier work, and the concentration of active sites has been effectively regulated.[50] It was a common and effective method to further regulate the active site and promote the catalytic activity through the combination of other elements; moreover, the relative quantitative identification of the active site for the ternary catalyst was still a challenging research. In this work, the Co element was combined into CuCe samples preparing a series of CuCoCe ternary catalysts by a coprecipitation method. The compositing effect of Co over Cu/Ce-based catalysts was studied by enhanced Raman, low-temperature DRIFTS technologies, and DFT calculation; further, the main active sites of CuCoCe ternary catalysts were relatively quantitatively tracked. By ternary composition, it is expected that further enhancement of catalytic activity and stability will achieve the conversion at lower temperatures for CO and toluene. In addition, binary CoCe and CoCu samples with different atomic ratios were prepared to discuss their effect and interaction in CuCoCe catalysts.

2. EXPERIMENTAL SECTION

2.1. Catalyst Preparation

All the reagents are used without further purification, and all of the catalysts are prepared by coprecipitation methods. During the precipitation reaction, the precipitation pH value is controlled by adjusting the drip rate of salt and alkali solution, which is continuously monitored by a pH meter, and the precipitation process pH is always maintained at 11. After aging for 2 h, the precipitate is repeatedly washed with distilled water and centrifuged until the pH dropped to 7, and the precursor (hydroxide) is obtained by drying at 80 °C for 12 h. Finally, the catalyst is successfully prepared by calcining the precursor at 350 °C with a heating ramp of 2 °C/min for 4 h in the muffle furnace. In this work, the subscripts *x*, *y*, and *z* represent the atomic ratio of Cu, Co, and Ce. The prepared salt solution and alkali solution are simultaneously dropped into a beaker containing 100 mL of deionized water by the peristaltic pump at a certain speed. The synthesis is performed and magnetically stirred in a beaker of water bath at 50 °C, and the schematic illustration of catalysts preparation is shown in Figure S1. In addition, the CuCe, CuCoCe, CoCe, and CoCu catalysts represent Cu_1Ce_3, $Cu_xCo_yCe_z$ (contains $Cu_1Co_{0.5}Ce_3$, $Cu_1Co_1Ce_3$, and $Cu_{0.5}Co_1Ce_3$ ternary catalysts), Co_yCe_z (contains Co_1Ce_7, Co_1Ce_3, and Co_1Ce_2 catalysts), and Co_yCu_x catalysts (contains Co_1Cu_7, Co_1Cu_3, and Co_1Cu_2), respectively. Pure oxide catalysts contain CuO, Co_3O_4, and CeO_2 catalysts. The three CuCoCe ($Cu_xCo_yCe_z$) catalysts with molar ratios of Cu, Co, and Ce of 1:0.5:3, 1:1:3, and 0.5:1:3 were denoted as $Cu_1Co_{0.5}Ce_3$, $Cu_1Co_1Ce_3$, and $Cu_{0.5}Co_1Ce_3$, respectively. A certain amount of $Cu(NO_3)_2{\cdot}3H_2O$ (Aladdin, AR grade), $Co(NO_3)_2{\cdot}6H_2O$(Macklin, AR grade), and $Ce(NO_3)_3{\cdot}6H_2O$ (Macklin, AR grade) were dissolved in 200 mL of deionized water to obtain a salt solution. Certain concentrations of NaOH (Aladdin, AR grade) and $NH_3{\cdot}H_2O$ (Macklin, AR grade) were dissolved in 100 mL of deionized water to obtain an alkali solution. In order to synthesize $Cu_1Co_{0.5}Ce_3$, 10 mmol of $Cu(NO_3)_2{\cdot}3H_2O$, 5 mmol of $Co(NO_3)_2{\cdot}6H_2O$, and 30 mmol of $Ce(NO_3)_3{\cdot}6H_2O$ were dissolved and mixed in deionized water as salt solutions. NaOH (molar ratio 1:2.25) and $NH_3{\cdot}H_2O$ were dissolved and mixed in deionized water as an alkali solution. Similarly, for $Cu_1Co_1Ce_3$ and $Cu_{0.5}Co_1Ce_3$, the concentrations of $Cu(NO_3)_2{\cdot}3H_2O$, $Co(NO_3)_2{\cdot}6H_2O$, and $Ce(NO_3)_3{\cdot}6H_2O$ in salt solution are, respectively, 10, 10, and 30 mmol and 5, 10, and 30 mmol. The alkali solution is the same as the $Cu_1Co_{0.5}Ce_3$ sample.

2.2. Catalyst Characterization

X-ray powder diffraction (XRD) patterns of the catalysts are performed on a Bruker D8 ADVANCE X-ray diffractometer with Cu Kα (λ = 1.5406 Å) radiation operated at 45 kV and 30Ma, and at a scan rate of 15° min^{-1} within the range of scattering angle 2θ of 10 to 90°. The Brunauer−Emmett−Teller (BET) and Barrett−Joyner−Halenda (BJH) pore size distributions of catalysts are characterized by N_2 adsorption−desorption measurement on a Micromeritics ASAP 2020 nitrogen physisorption device at −196 °C. Before the tests, the catalysts are degassed at 300 °C for 7 h to remove physically adsorbed impurities. The morphologies and texture of catalysts are investigated

https://doi.org/10.1021/jacsau.4c01221
JACS Au 2025, 5, 975−989

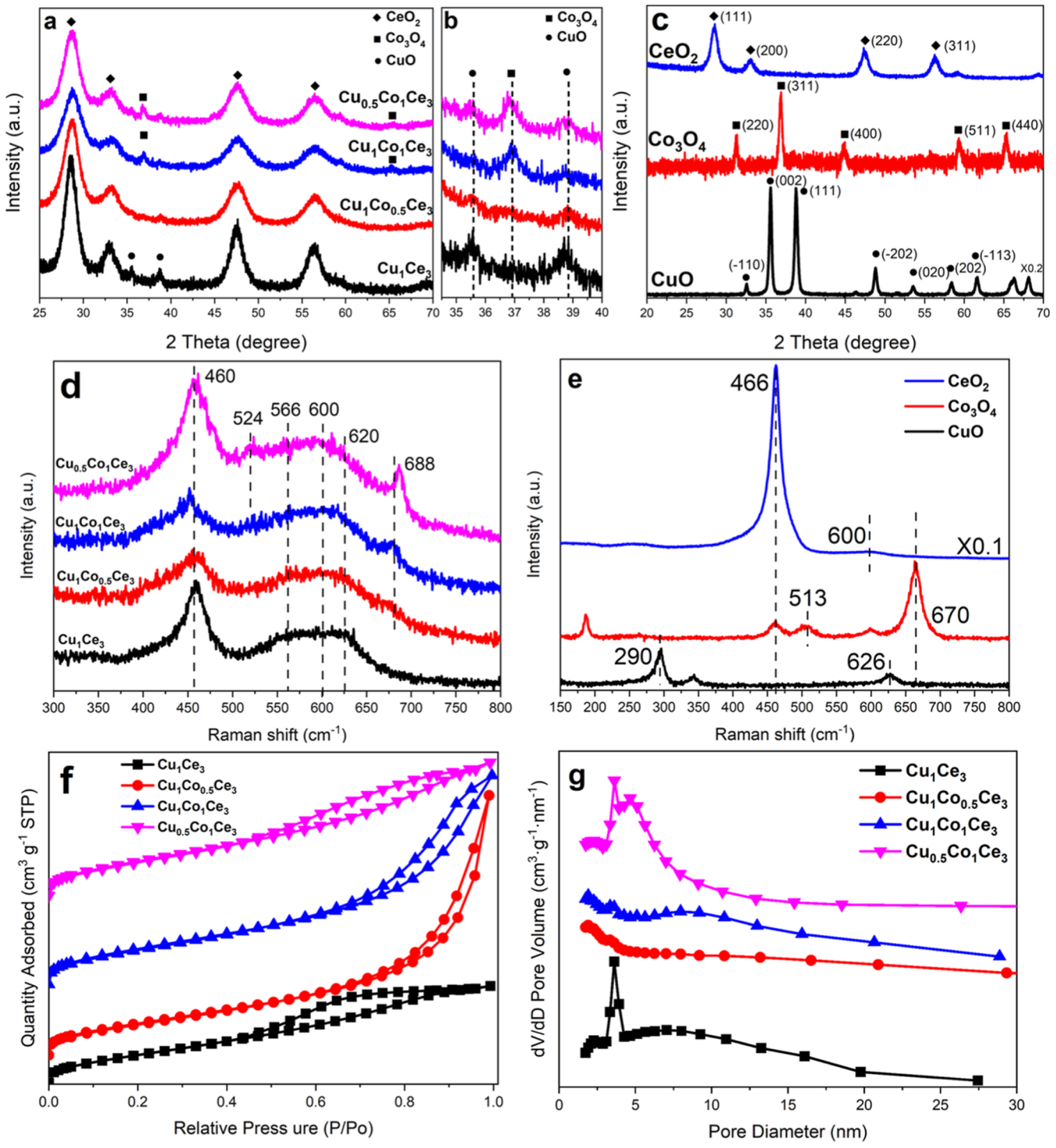

Figure 1. XRD profiles (a−c) and Raman spectroscopy (d,e) of CuCoCe catalysts and pure oxide samples; (b) local enlargement of (a). N_2 sorption isotherms (f) and pore size distributions (g) of the CuCoCe catalysts.

using scanning electron microscopy (SEM, Gemini SEM 500, 3KV) and transmission electron microscopy (TEM, Talos L120C, 200 kV), and in characterization of TEM, the powder samples are dispersed and sonicated in alcohol, and then they are dropped on an ultrathin carbon film coated on a Cu grid. The hydrogen temperature-programmed reduction (H_2-TPR) of catalysts is tested on an Automatic chemical adsorption instrument (Autochem 2920, MICROMERITICS) with 50 mg catalysts in a U-shaped quartz reactor; after the preheat treatment in 5% O_2/He flow from 30 to 300 °C, it is held for 1 h at the flow velocity of 30 mL min^{-1}, and then it is cooled to 30 °C with Ar purging at the flow velocity of 30 mL min^{-1}. In the end, the catalysts are reduced from 30 to 800 °C with the 5% H_2/Ar at a constant rate of 10 °C min^{-1} under a gas flow of 30 mL min^{-1}. The oxygen temperature-programmed desorption (O_2-TPD) also is measured on an Automatic chemical adsorption instrument (Autochem 2920, MICROMERITICS). 50 mg of the catalysts with 50 mg is preheated in He under the flow of 30 mL min^{-1} from 30 to 300 °C; after holding for 1 h, it is cooled to 30 °C; and then it is purged in 5% O_2/He at the flow velocity of 30 mL min^{-1} for 1 h. At last, the catalysts are heated from 30 to 800 °C at 10 °C min^{-1} in He

https://doi.org/10.1021/jacsau.4c01221
JACS Au 2025, 5, 975−989

under a gas flow of 30 mL min^{-1}. The surface oxygen vacancy structure of the catalyst was characterized by an electron paramagnetic resonance (EPR) spectrometer (A300 BRUKER). The powder catalyst is dried at a constant temperature of 200 °C in a drying oven for 3 h to remove water vapor and other impurities adsorbed on the surface. The dried catalyst was loaded into the EPR quartz sample tube at 100 mg. Then, the EPR tube equipped with catalyst was placed into the detection cavity, and the EPR spectra were collected at the microwave bridge frequency of 9.32 GHz, temperature of −198 °C, and microwave power of 18 mW. X−ray photoelectron spectroscopy (XPS) measurement is performed on an XLESCALAB 250Xi electron spectrometer with monochromatic Al Ka (1486.6 eV) radiation, and the binding energy is calibrated based on the C 1s peaks at 284.8 eV. Raman spectroscopy is measured in a LabRAM HR system from HORIBA Scientific, and the objective of ×50−05 is used with the visible Raman spectra of 532 nm within the range of 100−1400 cm^{-1} at a spectral resolution of 1 cm^{-1} in a grating of 1800 gr/mm. In addition, enhanced visible light technology was used to characterize the surface Raman information on the catalyst to reduce the destruction of the asymmetric coordination structure of the catalyst surface by concentrated light energy.

2.3. Catalytic Activity Evaluation

The concentration of the reaction gas is monitored online by gas chromatography on a GC-2014C from Shimadzu. The catalytic activity of catalysts is tested in a fixed-bed quartz tubular microreactor of Φ = 10 mm with 0.1 g of catalyst of 40−60 mesh and 0.4 g of quartz sands. Either the 1000 ppm toluene +20 vol % O_2/N_2 Bal or 1 vol % CO + 20% vol.O_2/N_2 Bal is the reactant gas of toluene and CO under a total continuous gas flow of 100 mL min^{-1} with temperature range of 170−320 °C for toluene and 30 to 200 °C for CO, and the constant WHSV (w8 hly space velocity) is calculated, which is 60,000 mL $gcat^{-1}$ h^{-1}.

3. RESULTS AND DISCUSSION

3.1. Analysis of Structure and Morphology of Cu/Ce-Based Catalysts

The XRD patterns of all of the CuCoCe catalysts, CuCe, CoCe, and CoCu samples, are shown in Figures 1 and S2. In Figure 1a,b, the characteristic peaks between 35 and 40° in the Cu_1Ce_3 catalyst are attributed to the (002) and (111) crystal faces of CuO, while the peaks intensity of $Cu_1Co_{0.5}Ce_3$ was greatly weakened, indicating that the addition of Co promoted the CuO dispersion.[52] A characteristic peak which was attributed to the (220) crystal face of Co_3O_4 appeared near 33° with the increase of Co content, suggesting that the increase in Co content gradually began to aggregate in large quantities.[53] Diffraction peaks of CuO and Co_3O_4 species are almost absent in the XRD pattern of a $Cu_1Co_{0.5}Ce_3$ catalyst, which can indicate that the absence of large agglomeration of Cu and Co species in a $Cu_1Co_{0.5}Ce_3$ catalyst promotes more interfaces which are conducive to the formation of asymmetric $M_1-O_x-M_2$ species between Cu and Ce. The XRD patterns of CoCe samples are shown in Figure S2a, and the diffraction peak of Co_3O_4 (220) crystal plane near 33° gradually appears and increases with the increase of Co content, indicating the gradual agglomeration of Co species. Similarly, in the CoCu samples (Figure S2b), this characteristic peak also gradually increases with the Co content. They correspond to the characteristic peaks of pure oxide (Figure 1c); both CoCe and CoCu samples are not shown interaction by XRD results, nor do they form a new crystal structure; all exist in the form of metal oxides.

Raman spectroscopy is one of the most effective technologies for the characterization of metal−oxygen bond vibrations and material structure. From Figure 1d, it can be seen that the vibration peak of the $Cu_1Co_{0.5}Ce_3$ catalyst near 460 cm^{-1} that was assigned to F_{2g} in CeO_2 was significantly reduced compared with the Cu_1Ce_3 sample, and the ASOv vibration peak at 566 cm^{-1} is almost unchanged.[50] The large shoulder peak near 600 cm^{-1} for Cu/Ce-based catalysts with different Co contents was fitted and is shown in Figure S3. The vibration peak at 566 cm^{-1} was assigned to the ASOv (Cu−O_V−Ce) in the Cu−Ce interface, and the other peaks at 603, 620 cm^{-1}, and around 670 cm^{-1} are the vibrational modes of Ce−O_V−Ce in CeO_2, the B_g^2 in CuO, and A_{1g} in Co_3O_4.[54−56] The relative concentration of ASOv was calculated by the area intensity ratio of the peak and expressed as A_{566}/A_{460} (area ratio at 566 to 460 cm^{-1}), as shown in Figure 3b and Table S1. The relative concentration of ASOv in the $Cu_1Co_{0.5}Ce_3$ catalyst was 0.72, which was significantly higher than that of the Cu_1Ce_3 sample (0.46), indicating the addition of Co promoted the increase of ASOv concentration, while it was gradually decreased with the increase of Co content. With the increase of Co content and the decrease of Cu content, the intensity of the F_{2g} characteristic peak increases, and the vibration mode intensity of Co_3O_4 located near 524 and 688 cm^{-1} increases. It is worth noting that the vibration modes of Co_3O_4 are located at 513 and 670 cm^{-1}(Figure 1e), while the Raman characteristic peaks of Co species in the CuCoCe catalyst significantly gradually blue shift in the direction of high displacement with the increase of Co content, causing its own lattice expansion. Raman spectra of CoCe and CoCu samples were tested in order to study the interaction between Co and Ce and Cu shown in Figure S2c,d. Similar to CuCoCe catalysts, the Raman vibration peaks of Co species in CoCe samples were blue-shifted to 524 and 688 cm^{-1}, and the F_{2g} vibration peaks near 460 cm^{-1} was not shifted (Figure S2c). For CoCu samples, the Raman vibration peak of Co species at 513 and 670 cm^{-1} was the same as the Co_3O_4, and there was no shift (Figure S 2d). This showed that the shift of Co vibration peaks in CuCoCe catalysts is caused by a Ce element, indicating that there is interaction between Cu−Ce and Co−Ce among the three elements, and there is no interaction between Cu and Co. Importantly, CuCe is more likely to form ASOv. However, there is no obvious ASOv Raman vibration mode in CoCe samples.

The N_2 adsorption−desorption isotherms and pore size distributions of Cu/Ce-based catalysts, pure oxide, and CoCe and CoCu samples are shown in Figures 1f,g and S4. In the isothermal curve, CeO_2, Cu_1Ce_3, and CoCe samples all showed a type IV adsorption pattern (Figures 1f and S4a,e), while CuO, Co_3O_4, and CoCu samples all showed a type III adsorption pattern (Figure S4c,e). Interestingly, CuCoCe catalysts have changed from type III to type IV adsorption pattern with the increase of Co content (Figure 1f), showing a great effect on the surface physical structure of Cu/Ce-based catalysts after compositing of Co. For the pore size distribution (Figure 1g), the micropores are transformed into mesopores with the increase of Co. The $Cu_1Co_{0.5}Ce_3$ catalyst was mainly distributed in the micropore structure of around 2 nm, while the $Cu_{0.5}Co_1Ce_3$ shows a mesoporous structure of 3 nm−10 nm. Meanwhile, the specific surface area (S_{BET}) of all samples is shown in Table S1. The S_{BET} of CuCoCe catalysts was effectively increased after Co recombination for $Cu_1Co_{0.5}Ce_3$ (145.3 m^2/g), showing a larger S_{BET} than Cu_1Ce_3(124.6 m^2/g), and the maximum S_{BET} at $Cu_1Co_1Ce_3$ was 157.4 m^2/g, attributed to the increase of mesoporous structure. In the CoCe samples, the pore size gradually increased with the

https://doi.org/10.1021/jacsau.4c01221
JACS Au 2025, 5, 975−989

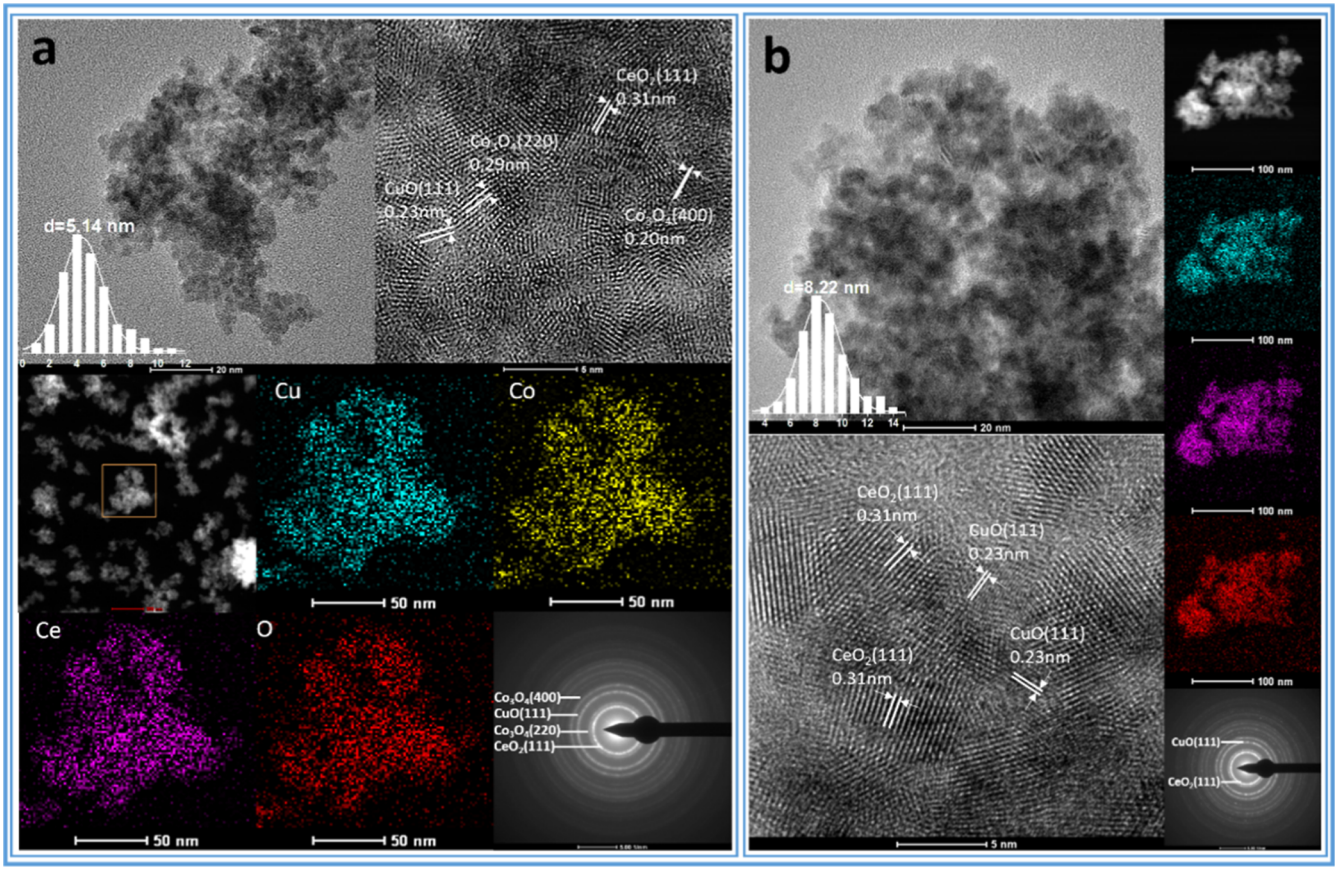

Figure 2. TEM, HRTEM, TEM-mapping and diffraction patterns spectrogram of $Cu_1Co_{0.5}Ce_3$ (a) and Cu_1Ce_3 (b) samples.

increase of Co (Figure S4b), while for CoCu samples, the pore size at 15 nm-60 nm increased with the increase of Co (Figure S 4d), because of Co_3O_4 (Figure S 4f) mainly in this interval.

The morphology, element distribution, particle size distribution, crystal planes and diffraction characteristics of the ternary $Cu_1Co_{0.5}Ce_3$ and binary Cu_1Ce_3, Co_1Ce_3, and Co_1Cu_3 samples were characterized by TEM, as shown in Figures 2 and S5. It was found by HRTEM calibration that CuO, Co_3O_4, and CeO_2 oxides existed both in the $Cu_1Co_{0.5}Ce_3$ catalyst and the binary samples, in accord with the XRD scanning results, and the exposed crystal faces of the three oxides were CuO (111), Co_3O_4 (220), Co_3O_4 (400), and CeO_2 (111), respectively.[38,41] After calculation of particle size distribution, the Cu_1Ce_3 sample shows spherical nanoclusters of about 8.22 nm CuO and CeO_2 forming a large number of Cu−Ce interfaces with abundant ASOv (Figure 2b). The $Cu_1Co_{0.5}Ce_3$ catalyst was diminished to about 5.14 nm after the composite of Co, which can help to generate more Cu−Ce interfaces and ASOv than Cu_1Ce_3, and there was higher dispersity in Cu than the Co element from the TEM-Mapping spectrogram (Figure 2a). These results showed that the addition of Co contributes to promotion of the dispersion of Cu and Ce forming more Cu−Ce interfaces to produce higher concentrations of ASOv. This also validates the conclusion of XRD, H_2-TPR, and Raman spectroscopy above. In the Co_1Ce_3 sample, the particle size of the oxide grows to about 9.76 nm (Figure S5a), while in the Co_1Cu_3 sample, the particle size were further increases and agglomerates to 14.83 nm (Figure S5b). The diffraction pattern of the Cu_1Ce_3, Co_1Ce_3, and specially Co_1Cu_3 sample shows a large number of bright spots compared with the smooth concentric circles of the $Cu_1Co_{0.5}Ce_3$ catalyst. This indicates that the recombination between oxides and oxides in the $Cu_1Co_{0.5}Ce_3$ ternary catalyst is better, which was more conducive to the formation of ASOv at the interface, and the higher crystallinity of Co_3O_4 and CuO in CoCu samples made it difficult to form interface and defect sites.

3.2. Redox and Oxygen Storage Properties of Cu/Ce-Based Catalysts

The reducibility, oxidizability, and the active components of the Cu/Ce-based catalysts were researched by H_2-TPR, and the active components were quantitatively analyzed on the basis of hydrogen consumption, as shown in Figures 3a,b and S6. From the Figure 3a, the α and β characteristic peaks at 121 and 149 °C were attributed to the reduction of highly dispersed CuO species and ASOv active species, respectively, and the corresponding hydrogen consumption is shown in Figure 3b and Table S1.[50] A $Cu_1Co_{0.5}Ce_3$ catalyst showed a significantly increased ASOv reduction peak compared to the Cu_1Ce_3 sample with a maximum corresponding hydrogen consumption of 2.43 mmol/g, while the area of the ASOv characteristic peak and hydrogen consumption decreases with the increase of Co content. This indicated that the moderate addition of Co promotes increases of ASOv concentration at the Cu−Ce interface and validates results of the Raman, EPR, and O_2-TPD. A new peak attributed to the reduction of a Co_3O_4 cluster appeared near 220 °C, and it is maximum in the $Cu_{0.5}Co_1Ce_3$ catalyst with the highest Co content. The results showed that an appropriate amount of Co in a CuCe catalyst can help to improve the dispersion of Cu and Ce species and generate more active species, but the increase of Co content

https://doi.org/10.1021/jacsau.4c01221
JACS Au 2025, 5, 975−989

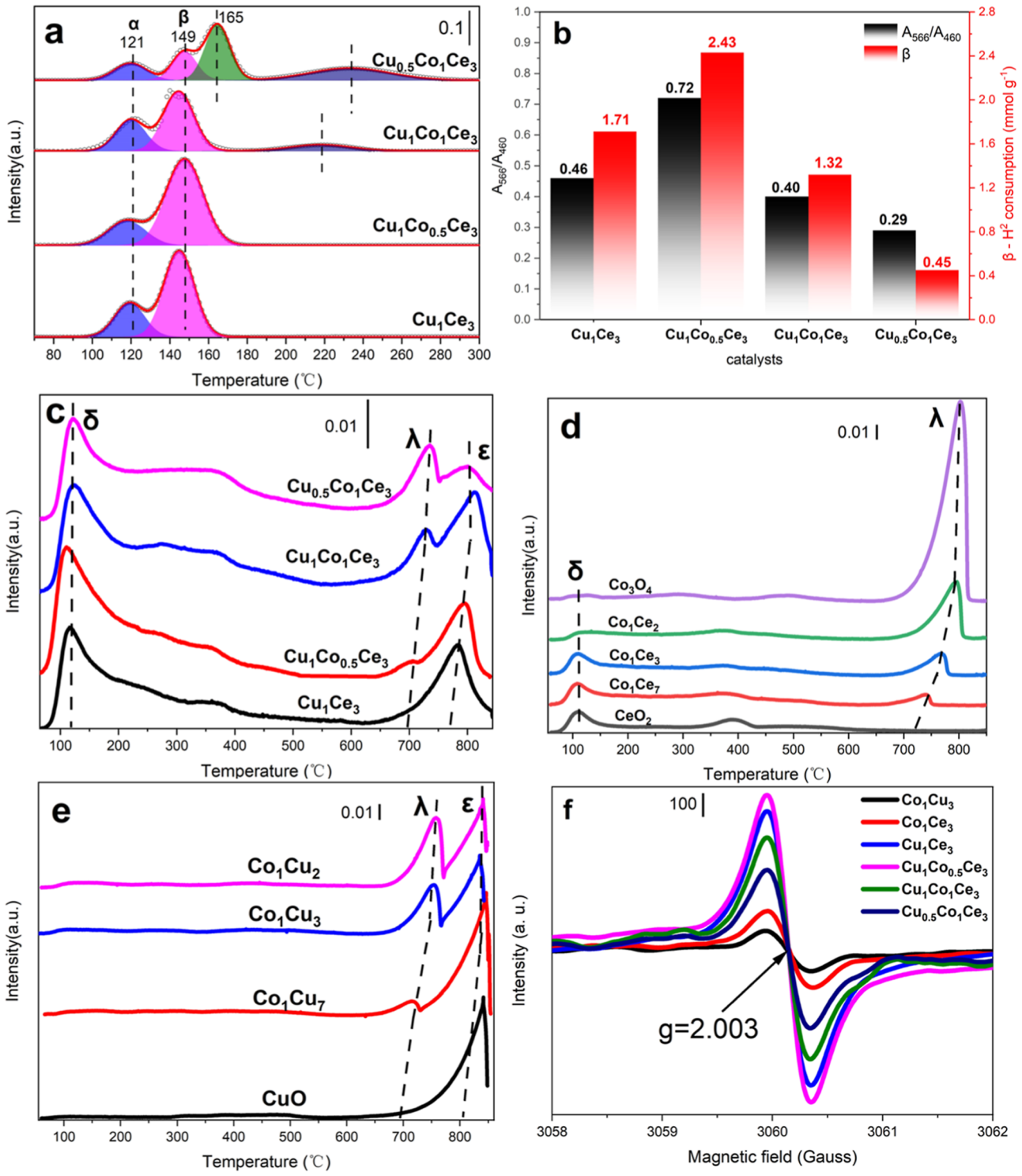

Figure 3. H_2-TPR curves for (a) CuCoCe catalysts. The concentration of the ASOv for CuCoCe catalysts from Raman (A_{566}/A_{460}) and H_2-TPR (H_2 consumption of β peak) (b). O_2-TPD curves of CuCoCe (c), CoCe (d), and CoCu (e) catalysts. EPR spectra (f) of the ternary and binary catalysts.

will intensify agglomeration of oxide and the decrease of active species. There are two reduction peaks (Figure S6a) in the CoCe sample similar to those of Co_3O_4 species, and there was the reduction of Co^{3+} to Co^{2+} in the low temperature region and the reduction of Co^{2+} to Co^0 in the high temperature region, respectively. This gradually shifts to high temperature with the increase of Co content, and the peak intensity also increases. It is worth noting that the reduction peak of Co−Ox−Ce species was not observed in the H_2-TPR curve of CoCe samples, suggesting difficult to form ASOv species at the Co−Ce interface. In CoCu samples (Figure S6b), reduction peaks at 122 and 160 °C are attributed to surface highly dispersed CuO and Co_3O_4 species, which corresponds to the reduction peak of the $Cu_{0.5}Co_1Ce_3$ catalyst at the corresponding temperatures (Figure 3a). With the increase of Co content, the reduction peaks of agglomerated CuO and Co_3O_4 species

https://doi.org/10.1021/jacsau.4c01221
JACS Au 2025, 5, 975−989

at 188 and 230 °C gradually expanded to higher temperature, indicating that the higher valence Cu and Co species was increased.

Surface oxygen vacancies and bulk phase structures of Cu/Ce-based catalysts were evaluated quantitatively by studying the adsorption and desorption behavior of oxygen in the catalyst surface and bulk phase. O_2-TPD is one of the most effective methods to characterize oxygen adsorption and desorption, and all spectrogram and oxygen desorption number of corresponding peaks are shown in Figure 3c−e and Table S1. Most of the δ peaks near 120 °C come from the adsorbed oxygen in ASOv and the peak in $Cu_1Co_{0.5}Ce_3$ with a maximum of 1.23 mmol/g of oxygen desorption amount than 0.70 mmol/g in Cu_1Ce_3 (Figure 3c), which further verifies that recombination of Co can promote the generation of ASOv.[50,57] With the increase of Co content, the intensity of the λ peak belonging to the desorption of the oxygen lattice in Co_3O_4 species near 700 °C increases gradually; meanwhile, the ε peak belonging to desorption of lattice oxygen in CuO species at 800 °C showed a trend of gradual decrease. In CoCe samples (Figure 3d), the intensity of the δ peak gradually decreases with the increase of Co content, indicating that the oxygen vacancies (δ characteristic peak) of CoCe samples originate from CeO_2, and there was no ASOv of the Co−O_V−Ce structure, which is consistent with the result of H_2-TPR. For the CoCu samples (Figure 3e), no characteristic peaks of surface adsorbed oxygen were found in the low temperature region; meanwhile, the λ and ε desorption peaks in the high temperature region were apparent corresponding to CuCoCe catalysts, and the λ and ε peaks show a trend of increased and decreased with the increase of Co and decrease of Cu content. The results indicated that the CoCu binary catalyst failed to form ASOv.

The relative oxygen vacancy contents of Co_1Ce_3, Co_1Cu_3, Cu_1Ce_3 and CuCoCe catalysts were further tested by EPR, as shown in Figure 3f. A symmetrical signal at 2.003G was attributed to the electrons trapped in oxygen vacancies.[36,58] A large number of oxygen vacancies were formed in Cu_1Ce_3 samples, which was mainly from ASOv at the Cu−Ce interface, while there was a stronger EPR signal in the $Cu_1Co_{0.5}Ce_3$ catalyst after combination of Co than Cu_1Ce_3, and the EPR signal was gradually decreased with the increase of Co. It is indicated that the appropriate addition of Co in a Cu/Ce-based catalyst could promote the generation of ASOv. It is primarily due to the addition of Co enhanced the dispersion of CuO and CeO_2 species forming a larger amount of Cu−Ce interface. The Co_1Ce_3 sample shows a weaker EPR signal, because a small amount of oxygen vacancy in CoCe comes from CeO_2. From EPR spectra of pure oxide (Figure S7), it can be seen that it contains almost no oxygen vacancies in the prepared Co_3O_4 and CuO samples because of their structural characteristics. This results in almost no oxygen vacancy signal for the Co_1Cu_3 sample. Therefore, the results of Raman and O_2-TPD characterization show that it is almost difficult to form ASOv in CoCe and CuC samples.

3.3. Analysis of Formation Energy of ASOv in Cu/Ce-Based Catalysts

DFT calculations have been used to study the formation energy of Cu−Ce ASOv (E_{ASOV}) at the interface between CuO and CeO_2 for CuCe and CuCoCe catalyst models, and all the models were constructed according to the main exposed crystal plane (111) of the CeO_2. The model exposed crystal plane was supported by XRD and HRTEM, and the (111) also was the most reported crystal plane for theoretical calculations of ceria-base materials. The formation of vacancy and calculation of formation energy was shown in detail in Supporting Information. As shown in Figures 4 (side view) and S8 and S9 (top and bottom view), the asymmetric Cu−Ox−Ce structure was formed at the Cu−Ce interface of the Cu/Ce-based catalyst (Figure 4a,c), and the recombination of cobalt oxide in the CuCoCe catalyst greatly affected the formation of ASOv at the Cu−Ox−Ce structure of the Cu−Ce interface. For the binary CuCe sample (Figure 4b), the E_{ASVO} was 1.502 eV through DFT calculations, while the CuCoCe catalyst reduced to 0.854 eV after the addition of cobalt (Figure 4d). The DFT calculations further evidence that the ASOv easier was formed in the CuCoCe catalyst. This conclusion also verifies the above characterization results that there is a higher concentration of ASOv activity sites in the CuCoCe catalyst after addition of appropriate Co species than in the CuCe sample.

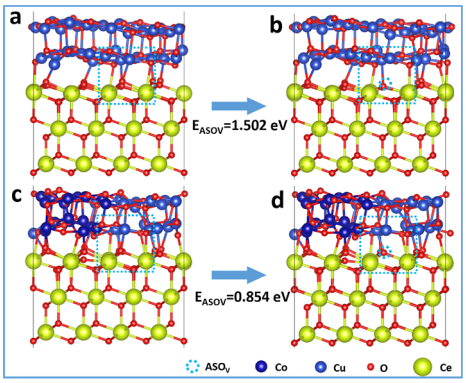

Figure 4. Formation energy by DFT conclusion of asymmetrical oxygen vacancy (ASOv) from the perfect side view model (a,c) to side view model (b,d) of ASOv formation over CuCe samples (a,b) and CuCoCe catalysts (c,d).

3.4. Analysis of Ion Valences and Content on Cu/Ce-Based Catalysts

The valence states and relative contents of surface elements of CuCoCe ternary catalysts and binary samples were characterized by XPS, and the fitting diagram and surface ion contents are shown in Figures 5 and S10, S11 and Table S2. Auger electron spectra (LMM) of Cu near at 917.1 and 914.7 eV, respectively, represent Cu^{2+} and Cu^{+} (Figure 5a).[9] The fitting calculation shows that the Cu^{+} concentration increases significantly from 41.3% in Cu_1Ce_3 to 46.4% of the $Cu_1Co_{0.5}Ce_3$ catalyst (Figure 5f). Many studies have shown that Cu^{+} was the composition of active site in Cu−Ce catalysts.[50] The Cu^{+} concentration decreases gradually with the increase of Co content in CuCoCe catalysts, indicating that the concentration of the active site containing Cu^{+} gradually decreases. The Cu 2p spectrum was also fitted (Figure 5b), and the concentration of Cu^{2+} and Cu^{+} was calculated by characteristic peaks located near 933.5 and 932.5 eV, which are almost similar to the calculated results of the Cu LMM spectrum. From Figure 5c, the Ce 3d spectrum near 904 and 885 eV shows that peak area intensity of Ce^{3+} in the $Cu_1Co_{0.5}Ce_3$ catalyst was significantly enhanced compared to Cu_1Ce_3, and the highest content was 20.3% for the $Cu_1Co_{0.5}Ce_3$ catalyst, with decreasing trend with increase of

https://doi.org/10.1021/jacsau.4c01221
JACS Au 2025, 5, 975−989

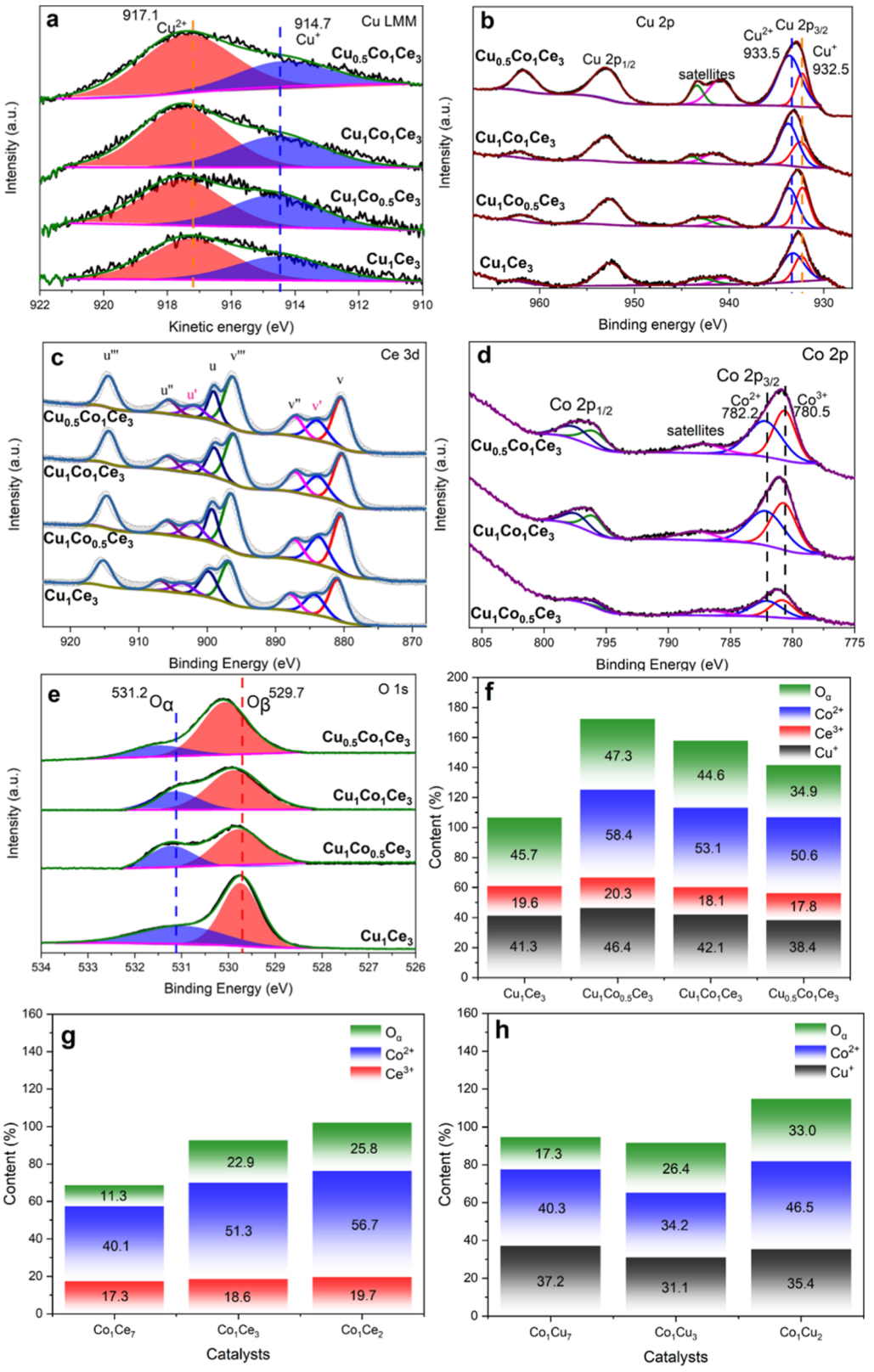

Figure 5. XPS spectra of CuCoCe catalysts in (a) Cu LMM, (b) Cu 2p, (c) Ce 3d, (d) Co 2p, and (e) O 1s region. Content of Cu^{+}, Ce^{3+}, Co^{2+}, and O_{α} in (f) CuCoCe, (g) CoCe, and (h) CoCu samples.

Co.[15] This peak position shifts toward the low binding energy, showing that the interaction between Cu and Ce was strengthened after the addition of Co, promoting the formation of Ce^{3+}. In CoCe samples, the content of Ce^{3+} was significantly increased with increase of Co content, and the peak position of Co_1Ce_2 shifted also toward the low binding energy, indicating that the increase of Co was conducive to the formation of Co−Ce interaction. In fitting spectra of Co

https://doi.org/10.1021/jacsau.4c01221
JACS Au 2025, 5, 975−989

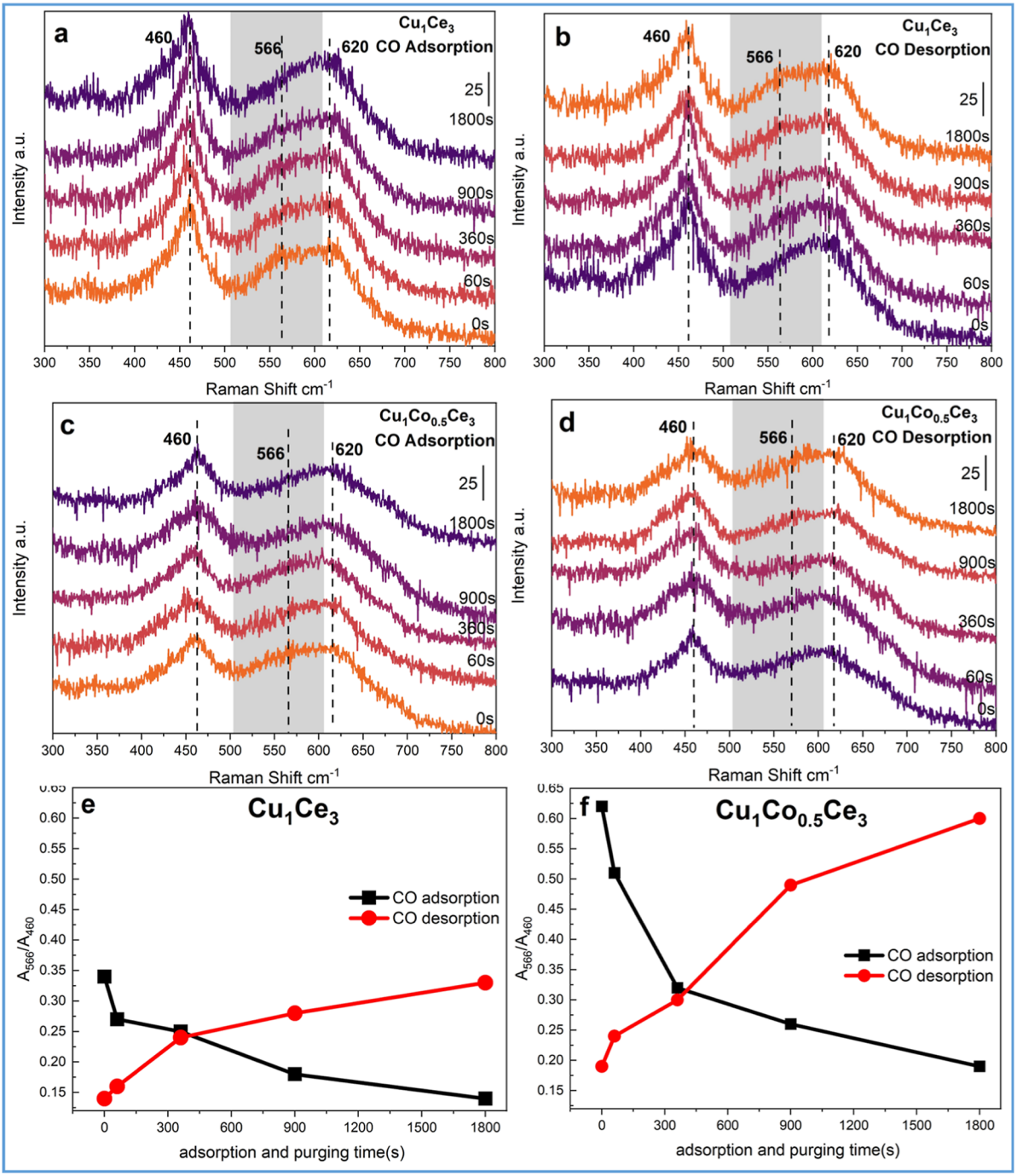

Figure 6. In-situ enhanced Raman spectrogram of CO adsorption−desorption in (a,b) Cu_1Ce_3 sample and (c,d) $Cu_1Co_{0.5}Ce_3$ catalyst. (e,f) Trend diagram of ASOv (A_{566}/A_{460}) with CO adsorption−desorption time in Cu_1Ce_3 and $Cu_1Co_{0.5}Ce_3$ catalysts by in-situ enhanced Raman.

species (Figure 5d), the binding energies near 781 and 782 eV were attributed to the Co^{3+} and Co^{2+}, respectively.[59] From Co $2p_{3/2}$, the Co^{2+} concentration was calculated and highest concentration was shown in the $Cu_1Co_{0.5}Ce_3$ catalyst (58.4%) (Figure 5f), and the weaker peak strength was attributed to relatively lower content of Co. The concentration of Co^{2+} showed an increasing trend in the CoCe samples (Figures 5g and S10a). Moreover, there was a trend of increasing after decreasing in CoCu samples (Figures 5h and S11c) with the lowest Co^{2+} content in the Co_1Cu_3 sample the same as the Cu^+. The CoCu samples exhibit a unique satellite peak (Figure S11a) located near 919.5 eV, which is associated with the agglomeration of CuO; meanwhile, the Cu 2p spectrum shows similar results (Figure S11b). Compared with CoCe (Figure S10a) and CoCu (Figure S11c) samples, the Co $2p_{3/2}$ spectrum in the CuCoCe (Figure 4d) catalysts is shifted by about 1 eV, which indicates that by adding Co to the CuCe sample, it was easier to enhance the Cu−Ce interaction. The O 1s spectrum can relatively quantify the surface oxygen vacancy concentration, and the O_α and O_β near 531 and 529 eV were the characteristic peaks of surface adsorbed oxygen and bulk lattice oxygen, respectively.[19,54] Both $Cu_{0.5}Co_1Ce_3$ (Figure 5e) and Co_1Cu_2 samples (Figure S11d) shift toward higher binding energy when the content of Co increases, meaning that their

https://doi.org/10.1021/jacsau.4c01221
JACS Au 2025, 5, 975−989

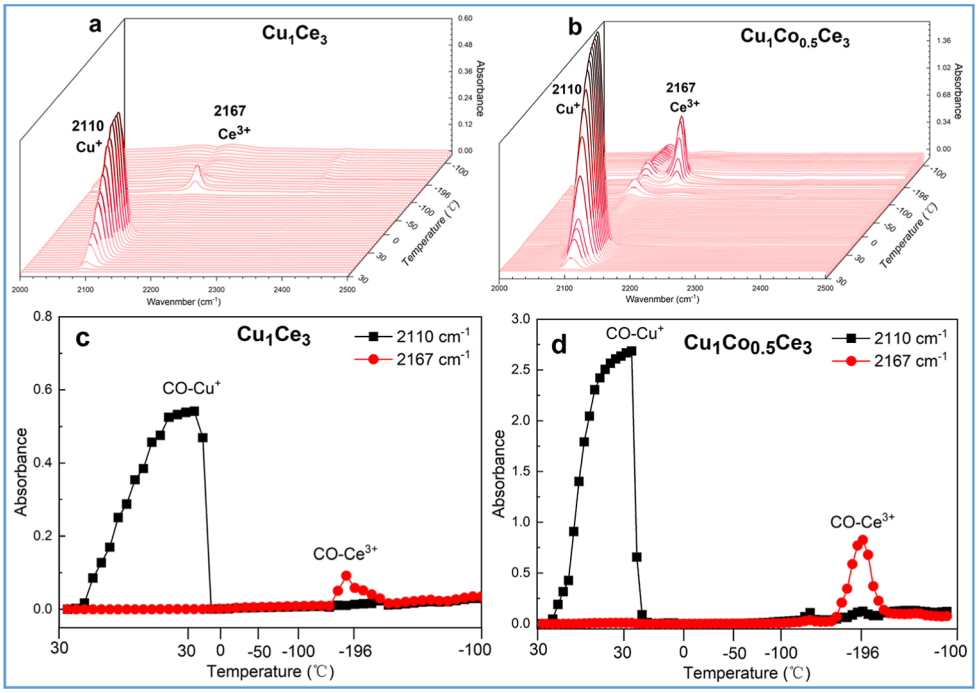

Figure 7. In-situ DRIFTS spectra of CO adsorption on (a) Cu_1Ce_3 and (b) $Cu_1Co_{0.5}Ce_3$ catalysts from 30 °C to −196 °C. The graphs of CO−Cu^+ and CO−Ce^{3+} adsorption intensity from 30 to −196 °C of (c) Cu_1Ce_3 and (d) $Cu_1Co_{0.5}Ce_3$ catalysts.

electron density was gradually decreased and the mobility of lattice oxygen was gradually increased. The maximum concentration of surface adsorbed oxygen was in the $Cu_1Co_{0.5}Ce_3$ catalyst (47.3%), more than in Cu_1Ce_3 (45.7%). Both the concentration of the corresponding ions (Cu^+, Ce^{3+}, and O_α) and Cu−Ce interaction of the $Cu_1Co_{0.5}Ce_3$ catalyst were increased after Co composite (Figure 5f). This indicates that recombination of Co significantly promoted the formation of ASOv, which further verifies the conclusions of Raman and H_2-TPR.

3.5. Tracking of Cu/Ce-Based Catalyst Activity Site by In-Situ Enhanced Raman

To explore the active sites of CuCoCe catalysts in the adsorption−desorption process for CO, the in-situ enhanced Raman tests are performed for the Cu_1Ce_3 and $Cu_1Co_{0.5}Ce_3$ catalysts in CO atmosphere, and the Raman spectrometer, UV-enhanced photosource, and in-situ cell are shown in Figure S12b,c,e. For the Cu_1Ce_3 sample (Figure 6a), a larger shoulder peak at near 600 cm^{-1} was fitted, as shown in Figure S13. The shoulder peak contains three peaks, which are ASO_V (Cu^+−O_V−Ce^{3+}) in the Cu−Ce interface at 566 cm^{-1}, the O_V (Ce^{3+}−O_V−Ce^{4+}) in CeO_2 at 603 cm^{-1}, and the characteristic peak of CuO at 620 cm^{-1}.[50] The intensity of ASO_V peak at 566 cm^{-1} was gradually weakened and almost disappeared after the 1800 s with the adsorption of CO, and it appeared gradually with the increase of desorption time shown in Figure 6a,b. These are attributed to the dynamic regeneration of ASOv active site after quantities of CO are adsorbed at the site and when CO was oxidized the original ASOv recovering. Studies have shown that the ASO_V active site at the Cu−Ce interface gradually exchanges to Cu^{2+}−O^{2-}−Ce^{4+} species (CO−Cu^+−O_V−Ce^{3+}+ O_2 → CO−Cu^{2+}−O^{2-}−Ce^{4+}) and the CO−Cu^{2+}−O^{2-}−Ce^{4+} species back to the original ASOv after the desorption of CO. Meanwhile, the same result was found in the $Cu_1Co_{0.5}Ce_3$ catalyst (Figure 6c,d), and the difference is there is a vibration peak of Co_3O_4 appearing near 688 cm^{-1} (Figure S14). From the fitting spectrogram of in-situ enhanced Raman at Cu_1Ce_3 and $Cu_1Co_{0.5}Ce_3$ catalysts (Figures S13 and S14), the concentration of ASOv was relatively quantified by the fitting peak area ratio (A_{566}/A_{460}), as shown in Figure 6e,f and Table S3 and S4. The initial ASOv concentration of the $Cu_1Co_{0.5}Ce_3$ catalyst was 0.62 much higher than that of the Cu_1Ce_3 sample (0.34) and decreased gradually from 0.62 to 0.19 after being adsorbed for 1800 s. Then, the concentration was gradually recovering from 0.19 to 0.60 after being desorbed 1800 s. According to the concentration trend with adsorption−desorption time, ASOv was the obvious active site in Cu/Ce-based catalysts, and the recombination of Co increased the ASOv concentration and promoted the reaction activity.

3.6. Tracking of Cu/Ce-Based Catalyst Active Sites by Ultralow-Temperature In-Situ DRIFTS

The infrared spectrum under ultralow-temperature conditions was sensitive to electronic structures of the binding sites in the CO adsorption−desorption and oxidation reaction; therefore, the reaction site of CO on a Cu/Ce-based catalyst was investigated by in-situ DRIFTS under ultralow-temperature conditions. An infrared spectrometer and ultralow-temperature in-situ cell are shown in Figure S12a,d. The in-situ DRIFTS test of the Cu_1Ce_3 and $Cu_1Co_{0.5}Ce_3$ catalysts in CO atmosphere from 30 to −196 °C is performed (Figure 7a,b). Both Cu_1Ce_3 and $Cu_1Co_{0.5}Ce_3$ displays a band at around 2110 cm^{-1} at 30 °C, which was attributed to the adsorption of CO on Cu^+ sites of ASOv, and the intensity of the CO−Cu^+ peak gradually increases with continuous adsorption.[50] With the decrease of temperature, the intensity of the CO−Cu^+ peak decreases until it disappears, indicating that CO is gradually being desorbed in this site. A band appears near 2117 cm^{-1} at −160 °C caused by the adsorption of CO on the Ce^{3+} site of ASOv, and the intensity of the CO−Ce^{3+} peak was the

https://doi.org/10.1021/jacsau.4c01221
JACS Au 2025, 5, 975−989

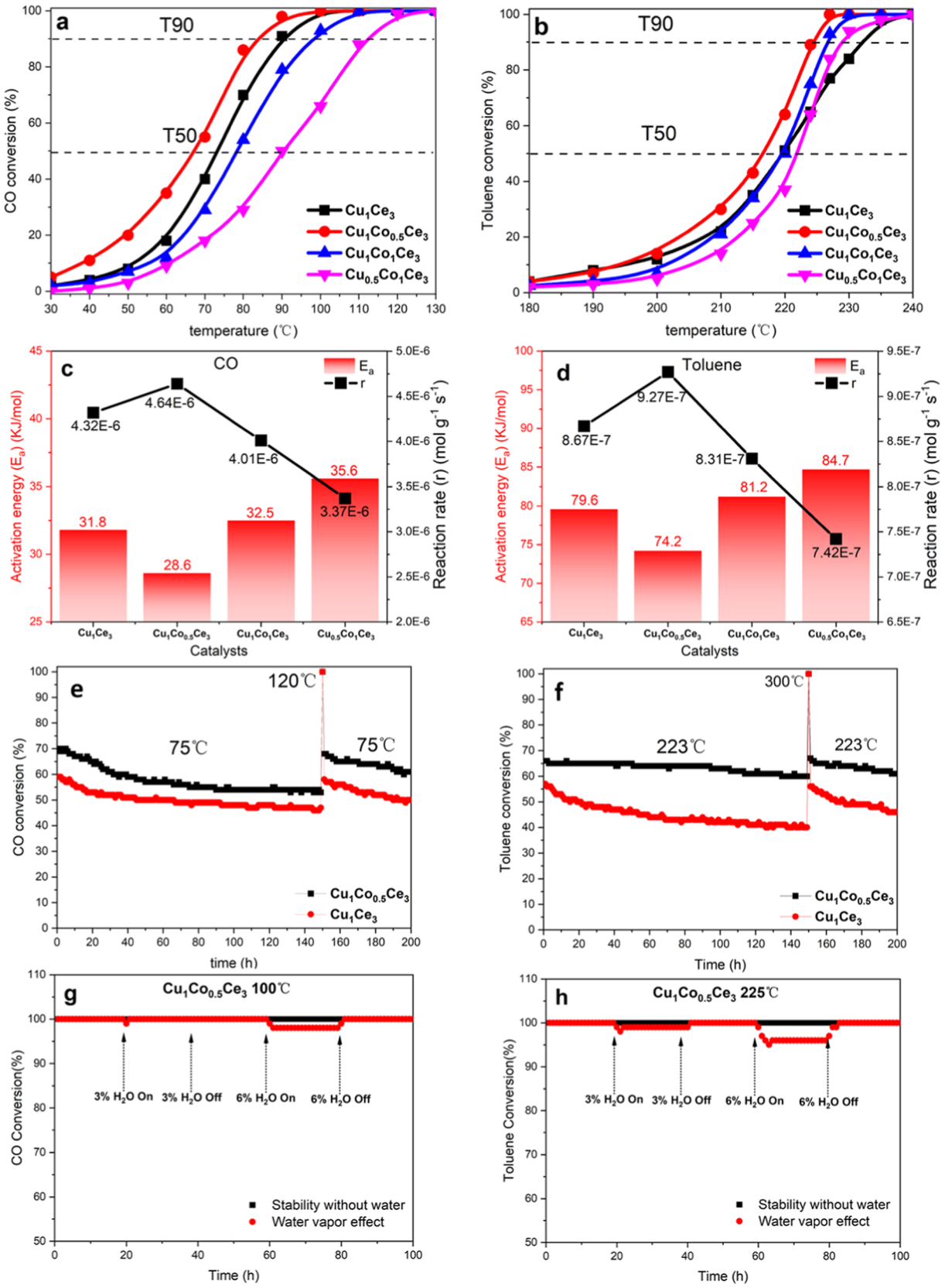

Figure 8. Conversions and corresponding Arrhenius plots of (a,c) CO and (b,d) toluene over Cu/Ce-based catalysts. Stability of the Cu_1Ce_3 and $Cu_1Co_{0.5}Ce_3$ catalysts for (e) CO and (f) toluene oxidation under 75 and 223 °C. Water vapor effect of the $Cu_1Co_{0.5}Ce_3$ catalyst for (g) CO and (h) toluene oxidation under 100 and 225 °C both in 3 vol % or 6 vol % H_2O. Reaction conditions: 0.1 g catalyst, 1 vol % CO, 20 vol % O_2 and WHSV = 60,000 mL g_{cat}^{-1} h^{-1} for CO oxidation; 0.1 g catalyst, 1000 ppm toluene, 20 vol % O_2 and WHSV = 60,000 mL g_{cat}^{-1} h^{-1} for toluene oxidation.

https://doi.org/10.1021/jacsau.4c01221
JACS Au 2025, 5, 975−989

maximum when the temperature is continuously reduced to −196 °C.[60] The intensity of the CO−Ce^{3+} peak gradually decreased and disappeared with temperature increases, indicating CO was gradually desorbed from the Ce^{3+} sites. The in-situ DRIFTS of Co_1Ce_3, Co_1Cu_3, and pure oxides CeO_2 and CuO samples was also performed from 30 to −196 °C, as shown in Figure S15. In these in-situ DRIFTS spectra of non-Cu/Ce-based samples, only the weak gaseous CO adsorption peak appeared at around 2160 cm^{-1}, and no adsorption peaks of CO−Cu^+ and CO−Ce^{3+} were found. Significantly, there were Cu^+ and Ce^{3+} on the non-Cu/Ce-based samples from the results of XPS, indicating that both CO−Cu^+ and CO−Ce^{3+} were at Cu^+−O_V−Ce^{3+} of the Cu−Ce interface, the ASOv active sites. The adsorption intensity trend of CO at Cu^+ and Ce^{3+} sites of ASOv with temperature over Cu_1Ce_3 and $Cu_1Co_{0.5}Ce_3$ catalysts is shown in Figure 7c,d. Compared with the Cu_1Ce_3 sample, the adsorption intensity of the $Cu_1Co_{0.5}Ce_3$ catalyst is higher both in Cu^+ and Ce^{3+} sites. It is worth noting that the desorption temperatures of CO from the Cu^+ site in Cu_1Ce_3 sample and $Cu_1Co_{0.5}Ce_3$ catalyst are 7 and 17 °C, respectively, indicating that CO is more easily desorbed on the $Cu_1Co_{0.5}Ce_3$ catalyst, which is beneficial to the reaction. Therefore, it can be concluded from the adsorption intensity at Cu^+ and Ce^{3+} sites that the ASO_V concentration of the $Cu_1Co_{0.5}Ce_3$ catalyst was more than that of the Cu_1Ce_3, which corresponds to that of the ASOv relative concentration difference over Cu_1Ce_3 and $Cu_1Co_{0.5}Ce_3$ catalysts by in-situ enhanced Raman.

3.7. Catalytic Activities of the Cu/Ce-Based Catalysts for the CO and VOC Oxidation

The structure−activity relationship of the Cu/Ce-based catalysts is explored by CO and toluene oxidation (Figure 8 and Table S5). Moreover, the activities of binary samples and pure oxidate for CO and toluene oxidation were also tested, as shown in Figure S17 and Table S6. The CuCoCe catalysts show excellent activity in CO oxidation, among which the conversion of $Cu_1Co_{0.5}Ce_3$ was 100% at 96 °C and superior to Cu_1Ce_3 (104 °C), showing an advantage of about 10 °C in T_{90}. The order of CO oxidation at Cu/Ce-based catalysts was $Cu_1Co_{0.5}Ce_3$ > Cu_1Ce_3 > $Cu_1Co_1Ce_3$ > $Cu_{0.5}Co_1Ce_3$, which corresponds to those of the concentrations of ASOv (Figures 3b and 5f). From the kinetics study (Figures 8c and S16), a $Cu_1Co_{0.5}Ce_3$ catalyst in CO oxidation showed the lowest activation energy and highest reaction rate with 28.6 kJ mol^{-1} and 4.64 × 10^{-6} mol^{-1} g^{-1} s^{-1}, respectively. It is attributed to the recombination of Co reducing the E_{ASOV}, so that ASOv was easier to be formed in the $Cu_1Co_{0.5}Ce_3$ catalyst; moreover, highly dispersed CuO species via the addition of Co thus forms more Cu−Ce interfaces, increasing the concentration of ASOv active site. The above DFT calculation and various characterization has confirmed this conclusion. Moreover, the increase of the specific surface area of the $Cu_1Co_{0.5}Ce_3$ catalyst compared to the Cu_1Ce_3 sample helps to expose more ASOv active sites. Activity of the CuCoCe catalyst decreased due to the decrease of ASOv concentration with the increase of Co content, and the addition of Co does not bring new active sites superior to Cu−Ce ASOv. Moreover, there is no direct evidence that Co−Ce and Co−Cu ASOv can be generated by comparing these binary samples. For toluene oxidation, the $Cu_1Co_{0.5}Ce_3$ catalyst still shows the best activity (Figure 8b) with 100% conversion at 227 °C, and the T_{90} activity is better than Cu_1Ce_3 with the increase of Co content. Therefore, the catalytic activities of the $Cu_1Co_{0.5}Ce_3$ catalyst increases significantly both in CO and toluene oxidation than Cu_1Ce_3. The results indicated that ASOv was the main active site in the CuCoCe catalyst for oxidation of both toluene and CO, but the Co species exhibited better activity for toluene than for CO mainly attributed to the additional Co^{2+} site that is beneficial to adsorption-activation performance for toluene. Furthermore, the prepared $Cu_1Co_{0.5}Ce_3$ catalyst compared with the reported studies shows performance advantages in both the conversion of CO and toluene (Table S8). In binary samples, Cu_1Ce_3 showed the best performance during both CO and toluene oxidation because the Cu−Ce ASOv active site was dominant. In contrast, CoCe and CoCu samples showed lower catalytic activity (Figure S17), which also verified the above characterization results that there was no ASOv site at the Co−Ce and Co−Cu interface, and their activity difference of different atomic ratios was related to the concentration of Co^{2+} and Cu^+, and the surface oxygen vacancy also has a greater promoting effect. Consequently, the formation and concentration of ASO_V is a key factor in the catalytic activity, which is consistent with the characterization results above in the work.

3.8. Catalytic Stability and Water Vapor Effect

In the long term catalytic stability test of CO oxidation at 75 °C (Figure 8e), the first 6 h conversion of $Cu_1Co_{0.5}Ce_3$ from 72% to 72% was far higher than that of the conversion of Cu_1Ce_3 from 59% to 55% because of more ASOv, and they were stabilized to 62% and 53% after 40 h, respectively. Carbon was gradually accumulated and covered the part of the active sites in the catalyst surface due to long-term incomplete conversion (<90%) that led to a declining conversion. However, the more serious decline of a $Cu_1Co_{0.5}Ce_3$ catalyst may be due to the agglomeration of Co species that did not form an interfacial structure, promoting the formation of carbon deposition. After the regeneration at 120 °C, the active site was re-exposed and the conversion was increased. For stability of toluene oxidation at 223 °C (Figure 8f), the $Cu_1Co_{0.5}Ce_3$ catalyst showed excellent stability, decreasing only by 4% after 150 h, while Cu_1Ce_3 almost decreased by 18% under the same condition. After in-situ regeneration at 300 °C, the activity returned to the initial state at 223 °C. It was found that the conversion increased significantly after regeneration at 300 °C, indicating that part of the aggregated CuO was reduced to form an isolated Cu^+ site at high temperature and declined gradually with time. This suggests that the isolated Cu^+ site was favorable and only effective in the short term because it was rapidly oxidated to the Cu^{2+} species. Stability and water vapor effect at the condition of complete conversion for CO (100 °C) and toluene (225 °C) was performed with the conversion of 100% after 100 h both in CO and toluene (Figure 8g,h). The water vapor has a great influence on toluene catalytic activity than CO, which was attributed to the adsorption and activation of CO on the Cu^+ sites of ASOv at the Cu−Ce interface, while the H_2O molecules and toluene were competitively adsorbed on the same Ce^{3+} sites of ASOv. After the water vapor is removed, the CO and toluene conversion is quickly recovered, exhibiting excellent long-term stability. The compositing of Co in the Cu/Ce-based catalyst improved the CO and toluene catalytic activity and stability, which was mainly due to the formation of more ASOv sites and decrease of carbon deposition compared to the CuCe sample; moreover, a small amount of Co^{2+} species dispersed on the

https://doi.org/10.1021/jacsau.4c01221
JACS Au 2025, 5, 975−989

$Cu_1Co_{0.5}Ce_3$ catalyst surface, providing additional active sites in toluene oxidation.

4. CONCLUSIONS

To summarize, a series of CuCoCe ternary catalysts were synthesized by recombination of Co in CuCe; meanwhile, CuCe, CoCe, and CoCu samples were prepared for comparison and analysis. Compared with all binary samples, the catalytic activity and stability of the $Cu_1Co_{0.5}Ce_3$ catalyst for CO and toluene was significantly improved, with T_{90} at 82 and 222 °C for CO and toluene, respectively. Active sites were confirmed and traced by a series of relatively quantified techniques, indicating that the addition of moderate Co in CuCe promoted the CuO dispersion and reduced the ASOv formation energy (E_{ASOV}), increasing the concentration of the ASOv active site in the Cu−Ce interface. In addition, the larger specific surface area and the additional Co^{2+} site were brought by moderate Co also conducive to improving the catalytic activity. The Cu−Ce interface was more likely to form the ASOv active site through comparison of CuCe, CoCe and CoCu binary samples, which was the main reason for the better performance in Cu/Ce-based catalysts. Both CoCe and CoCu show metal interactions, while there was no evidence that they could producing ASOv. The superior activity of CoCu over CoCe is due to the stronger Co−Cu interaction generating more Co^{2+} sites. Highly dispersed Co species were easy to form more Co^{2+} sites that were more favorable to the catalytic activity of CO and toluene than symmetrical oxygen vacancy, and this site was conducive to adsorption and oxidation of toluene than CO. It has been shown that the highly dispersed Cu^+ and Co^{2+} sites on the surface of the CoCe and CuCo can provide activity, but their catalytic activity is far lower than that of the ASOv active sites formed on the Cu/Ce-based catalysts. This work reveals the combination effect of cobalt in Cu/Ce-based catalysts, and the ASOv active sites in the Cu−Ce interface were explored relatively quantitatively by multiple in-situ enhanced and ex-situ characterization techniques.

■ ASSOCIATED CONTENT

Supporting Information

The Supporting Information is available free of charge at https://pubs.acs.org/doi/10.1021/jacsau.4c01221.

Detailed information on binary and pure oxides samples preparation, in-situ characterizations, DFT calculations, catalytic performance, DFT calculation, XRD patterns spectra, N_2 adsorption−desorption isotherms, pore size distributions, HRTEM and Mapping images, Raman fitting results, H_2-TPR, O_2-TPD, EPR, XPS, in-situ equipment diagram, in-situ DRIFTS, Arrhenius plots, conversion of CO and toluene, and supplementary tables and references (PDF)

■ AUTHOR INFORMATION

Corresponding Author

Daiqi Ye − *National Engineering Laboratory for VOCs Pollution Control Technology and Equipment, Guangdong Provincial Key Laboratory of Atmospheric Environment and Pollution Control, School of Environment and Energy, South China University of Technology, Guangzhou 510006, China;* orcid.org/0000-0001-9919-990X; Email: cedqye@scut.edu.cn

Authors

Jin Zhang − *Faculty of Environmental Science and Engineering, Kunming University of Science and Technology, Kunming 650500, China; National Engineering Laboratory for VOCs Pollution Control Technology and Equipment, Guangdong Provincial Key Laboratory of Atmospheric Environment and Pollution Control, School of Environment and Energy, South China University of Technology, Guangzhou 510006, China;* orcid.org/0009-0009-8775-4510

Hongyu Lin − *Faculty of Environmental Science and Engineering, Kunming University of Science and Technology, Kunming 650500, China*

Xiaoqin Zhang − *Faculty of Environmental Science and Engineering, Kunming University of Science and Technology, Kunming 650500, China*

Mingli Fu − *National Engineering Laboratory for VOCs Pollution Control Technology and Equipment, Guangdong Provincial Key Laboratory of Atmospheric Environment and Pollution Control, School of Environment and Energy, South China University of Technology, Guangzhou 510006, China;* orcid.org/0000-0002-7678-1953

Complete contact information is available at: https://pubs.acs.org/10.1021/jacsau.4c01221

Author Contributions

J. Zhang conceived the project and performed the all of the experiments, designed and analyzed DFT, in-situ enhanced Raman, and in-situ ultralow-temperature DRIFTS, and wrote the first draft and subsequent revisions. H. Lin carried out data processing and discussion and contributed to manuscript polishing. X. Zhang contributed to manuscript embellishment. M. Fu made critical suggestions to the manuscript. D. Ye supervised and directed the research. All authors have given approval to the final version of the manuscript. CRediT: **jin zhang** conceptualization, data curation, formal analysis, funding acquisition, investigation, writing - original draft, writing - review & editing.

Notes

The authors declare no competing financial interest.

■ ACKNOWLEDGMENTS

This work was financially supported by National Natural Science Foundation of China (22476054).

■ REFERENCES

(1) Mandal, S.; Thakur, M. A city-based PM2.5 forecasting framework using Spatially Attentive Cluster-based Graph Neural Network model. *J. Cleaner Prod.* **2023**, *405*, 137036.

(2) Fuller, R.; Landrigan, P. J.; Balakrishnan, K.; Bathan, G.; Bose-O'Reilly, S.; Brauer, M.; Caravanos, J.; Chiles, T.; Cohen, A.; Corra, L.; Cropper, M.; Ferraro, G.; Hanna, J.; Hanrahan, D.; Hu, H.; Hunter, D.; Janata, G.; Kupka, R.; Lanphear, B.; Lichtveld, M.; Martin, K.; Mustapha, A.; Sanchez-Triana, E.; Sandilya, K.; Schaefli, L.; Shaw, J.; Seddon, J.; Suk, W.; Téllez-Rojo, M. M.; Yan, C. Pollution and health: a progress update. *Lancet Planet Health.* **2022**, *6*, e535−e547.

(3) Huang, R.-J.; Zhang, Y.; Bozzetti, C.; Ho, K.-F.; Cao, J.-J.; Han, Y.; Daellenbach, K. R.; Slowik, J. G.; Platt, S. M.; Canonaco, F.; Zotter, P.; Wolf, R.; Pieber, S. M.; Bruns, E. A.; Crippa, M.; Ciarelli,

G.; Piazzalunga, A.; Schwikowski, M.; Abbaszade, G.; Schnelle-Kreis, J.; Zimmermann, R.; An, Z.; Szidat, S.; Baltensperger, U.; Haddad, I. E.; Prévôt, A. S. H. High secondary aerosol contribution to particulate pollution during haze events in China. *Nature* **2014**, *514*, 218−222.
(4) Wei, L.; Yu, C.; Yang, K.; Fan, Q.; Ji, H. Recent advances in VOCs and CO removal via photothermal synergistic catalysis. *Chin. J. Catal.* **2021**, *42*, 1078−1095.
(5) Li, Q.; Li, X.; Jiang, J.; Duan, L.; Ge, S.; Zhang, Q.; Deng, J.; Wang, S.; Hao, J. Semi-coke briquettes: towards reducing emissions of primary PM2.5, particulate carbon, and carbon monoxide from household coal combustion in China. *Sci. Rep.* **2016**, *6*, 19306.
(6) Feng, Y.; Dai, L.; Wang, Z.; Peng, Y.; Duan, E.; Liu, Y.; Jing, L.; Wang, X.; Rastegarpanah, A.; Dai, H.; Deng, J. Photothermal Synergistic Effect of Pt1/CuO-CeO2 Single-Atom Catalysts Significantly Improving Toluene Removal. *Environ. Sci. Technol.* **2022**, *56*, 8722−8732.
(7) Gan, T.; Yang, J.; Morris, D.; Chu, X.; Zhang, P.; Zhang, W.; Zou, Y.; Yan, W.; Wei, S. H.; Liu, G. Electron donation of non-oxide supports boosts O2 activation on nano-platinum catalysts. *Nat. Commun.* **2021**, *12*, 2741.
(8) Wang, A.; Lindgren, K.; Di, M.; Bernin, D.; Carlsson, P.-A.; Thuvander, M.; Olsson, L. Insight into hydrothermal aging effect on Pd sites over Pd/LTA and Pd/SSZ-13 as PNA and CO oxidation monolith catalysts. *Appl. Catal., B* **2020**, *278*, 119315.
(9) Zhang, X. M.; Tian, P. F.; Tu, W. F.; Zhang, Z. Z.; Xu, J.; Han, Y. F. Tuning the Dynamic Interfacial Structure of Copper-Ceria Catalysts by Indium Oxide during CO Oxidation. *ACS Catal.* **2018**, *8*, 5261−5275.
(10) Zhao, Y.; Jalal, A.; Uzun, A. Interplay between Copper Nanoparticle Size and Oxygen Vacancy on Mg-Doped Ceria Controls Partial Hydrogenation Performance and Stability. *ACS Catal.* **2021**, *11*, 8116−8131.
(11) Li, M.; Bi, F.; Xu, Y.; Hao, P.; Xiang, K.; Zhang, Y.; Chen, S.; Guo, J.; Guo, X.; Ding, W. Effect of Residual Chlorine on the Catalytic Performance of Co3O4 for CO Oxidation. *ACS Catal.* **2019**, *9*, 11676−11684.
(12) Zeng, Y.; Wang, Y.; Song, F.; Zhang, S.; Zhong, Q. The effect of CuO loading on different method prepared CeO2 catalyst for toluene oxidation. *Sci. Total Environ.* **2020**, *712*, 135635.
(13) Zeng, Y.; Haw, K. G.; Wang, Z.; Wang, Y.; Zhang, S.; Hongmanorom, P.; Zhong, Q.; Kawi, S. Double redox process to synthesize CuO-CeO2 catalysts with strong Cu-Ce interaction for efficient toluene oxidation. *J. Hazard. Mater.* **2021**, *404*, 124088.
(14) Davó-Quiñonero, A.; Bailón-García, E.; López-Rodríguez, S.; Juan-Juan, J.; Lozano-Castelló, D.; García-Melchor, M.; Herrera, F. C.; Pellegrin, E.; Escudero, C.; Bueno-López, A. Insights into the Oxygen Vacancy Filling Mechanism in CuO/CeO2 Catalysts: A Key Step Toward High Selectivity in Preferential CO Oxidation. *ACS Catal.* **2020**, *10*, 6532−6545.
(15) Yu, J.; Guo, Q.; Xiao, X.; Mao, H.; Mao, D.; Yu, J. High-heat treatment enhanced catalytic activity of CuO/CeO2 catalysts with low CuO content for CO oxidation. *Catal. Sci. Technol.* **2020**, *10*, 5256−5266.
(16) May, Y. A.; Wang, W.-W.; Yan, H.; Wei, S.; Jia, C.-J. Insights into facet-dependent reactivity of CuO−CeO2 nanocubes and nanorods as catalysts for CO oxidation reaction. *Chin. J. Catal.* **2020**, *41*, 1017−1027.
(17) Guo, X.; Ye, W.; Ma, T. Investigation of the re-dispersion of matrix Cu species in CuxCe1−xO2 nanorod catalysts and its effect on the catalytic performance in CO-PROX. *Catal. Sci. Technol.* **2020**, *10*, 4766−4775.
(18) Gao, Y.; Zhang, Z.; Li, Z.; Huang, W. Understanding morphology-dependent CuO -CeO2 interactions from the very beginning. *Chin. J. Catal.* **2020**, *41*, 1006−1016.
(19) Lu, J.; Wang, J.; Zou, Q.; He, D.; Zhang, L.; Xu, Z.; He, S.; Luo, Y. Unravelling the Nature of the Active Species as well as the Doping Effect over Cu/Ce-Based Catalyst for Carbon Monoxide Preferential Oxidation. *ACS Catal.* **2019**, *9*, 2177−2195.
(20) Kim, B. S.; Kim, P. S.; Bae, J.; Jeong, H.; Kim, C. H.; Lee, H. Synergistic Effect of Cu/CeO(2) and Pt-BaO/CeO(2) Catalysts for a Low-Temperature Lean NO (x) Trap. *Environ. Sci. Technol.* **2019**, *53*, 2900−2907.
(21) Liu, X.; Jia, S.; Yang, M.; Tang, Y.; Wen, Y.; Chu, S.; Wang, J.; Shan, B.; Chen, R. Activation of subnanometric Pt on Cu-modified CeO2 via redox-coupled atomic layer deposition for CO oxidation. *Nat. Commun.* **2020**, *11*, 4240.
(22) Hernández, J. A.; Gómez, S. A.; Zepeda, T. A.; Fierro-González, J. C.; Fuentes, G. A. Insight into the Deactivation of Au/CeO2Catalysts Studied by In Situ Spectroscopy during the CO-PROX Reaction. *ACS Catal.* **2015**, *5*, 4003−4012.
(23) Cargnello, M.; Doan-Nguyen, V. V.; Gordon, T. R.; Diaz, R. E.; Stach, E. A.; Gorte, R. J.; Fornasiero, P.; Murray, C. B. Control of metal nanocrystal size reveals metal-support interface role for ceria catalysts. *Science* **2013**, *341*, 771−773.
(24) Du, P. P.; Wang, W. W.; Jia, C. J.; Song, Q. S.; Huang, Y. Y.; Si, R. Effect of strongly bound copper species in copper-ceria catalyst for preferential oxidation of carbon monoxide. *Appl. Catal., A* **2016**, *518*, 87−101.
(25) Wang, W. W.; Du, P. P.; Zou, S. H.; He, H. Y.; Wang, R. X.; Jin, Z.; Shi, S.; Huang, Y. Y.; Si, R.; Song, Q. S.; Jia, C. J.; Yan, C. H. Highly Dispersed Copper Oxide Clusters as Active Species in Copper-Ceria Catalyst for Preferential Oxidation of Carbon Monoxide. *ACS Catal.* **2015**, *5*, 2088−2099.
(26) Jia, A. P.; Jiang, S. Y.; Lu, J. Q.; Luo, M. F. Study of Catalytic Activity at the CuO-CeO2 Interface for CO Oxidation. *J. Phys. Chem. C* **2010**, *114*, 21605−21610.
(27) Yang, W.; Wang, X.; Song, S.; Zhang, H. Syntheses and Applications of Noble-Metal-free CeO2-Based Mixed-Oxide Nanocatalysts. *Chem.* **2019**, *5*, 1743−1774.
(28) Liu, B.; Li, C.; Zhang, G.; Yao, X.; Chuang, S. S. C.; Li, Z. Oxygen Vacancy Promoting Dimethyl Carbonate Synthesis from CO2 and Methanol over Zr-Doped CeO2 Nanorods. *ACS Catal.* **2018**, *8*, 10446−10456.
(29) Esch, F.; Fabris, S.; Zhou, L.; Montini, T.; Africh, C.; Fornasiero, P.; Comelli, G.; Rosei, R. Electron localization determines defect formation on ceria substrates. *Science* **2005**, *309*, 752−755.
(30) Yu, K.; Lei, D.; Feng, Y.; Yu, H.; Chang, Y.; Wang, Y.; Liu, Y.; Wang, G.-C.; Lou, L.-L.; Liu, S.; Zhou, W. The role of Bi-doping in promoting electron transfer and catalytic performance of Pt/3DOM-Ce1−Bi O2−*δ*. *J. Catal.* **2018**, *365*, 292−302.
(31) Zhao, S.; Kang, D.; Liu, Y.; Wen, Y.; Xie, X.; Yi, H.; Tang, X. Spontaneous Formation of Asymmetric Oxygen Vacancies in Transition-Metal-Doped CeO2 Nanorods with Improved Activity for Carbonyl Sulfide Hydrolysis. *ACS Catal.* **2020**, *10*, 11739−11750.
(32) Shi, J.; Li, H.; Genest, A.; Zhao, W.; Qi, P.; Wang, T.; Rupprechter, G. High-performance water gas shift induced by asymmetric oxygen vacancies: Gold clusters supported by ceria-praseodymia mixed oxides. *Appl. Catal., B* **2022**, *301*, 120789.
(33) Dvořák, F.; Szabová, L.; Johánek, V.; Farnesi Camellone, M.; Stetsovych, V.; Vorokhta, M.; Tovt, A.; Skála, T.; Matolínová, I.; Tateyama, Y.; Mysliveček, J.; Fabris, S.; Matolín, V. Bulk Hydroxylation and Effective Water Splitting by Highly Reduced Cerium Oxide: The Role of O Vacancy Coordination. *ACS Catal.* **2018**, *8*, 4354−4363.
(34) Schweke, D.; Mordehovitz, Y.; Halabi, M.; Shelly, L.; Hayun, S. Defect Chemistry of Oxides for Energy Applications. *Adv. Mater.* **2018**, *30*, 1706300.
(35) Park, Y.; Kim, S. K.; Pradhan, D.; Sohn, Y. Surface treatment effects on CO oxidation reactions over Co, Cu, and Ni-doped and codoped CeO2 catalysts. *Chem. Eng. J.* **2014**, *250*, 25−34.
(36) Wang, X. Y.; Li, X. Y.; Mu, J. C.; Fan, S. Y.; Wang, L.; Gan, G. Q.; Qin, M. C.; Li, J.; Li, Z. Y.; Zhang, D. K. Facile Design of Highly Effective CuCexCo1-xOy Catalysts with Diverse Surface/Interface Structures toward NO Reduction by CO at Low Temperatures. *Ind. Eng. Chem. Res.* **2019**, *58*, 15459−15469.

https://doi.org/10.1021/jacsau.4c01221
JACS Au 2025, 5, 975−989

(37) Bae, J.; Kim, B.-S.; Jeong, H.; Lee, H. Mn-doped CuO Co3O4CeO2 catalyst with enhanced activity and durability for hydrocarbon oxidation. *Mol. Catal.* **2019**, *467*, 9−15.
(38) Jie, S.; Lin, X.; Chao, Z.; Liu, Z. Effective ternary copper-cerium-cobalt catalysts synthesized via a modified pechini method for selective oxidation of ethylbenzene. *Mater. Chem. Phys.* **2018**, *214*, 239−246.
(39) Chu, W.; Liu, Y.; Wang, H.; Cai, R.; Yang, W. Highly Efficient Removal of CO in Effluent Streams from Real-Life Propane Oxidation Process over CuO-CeO2-Based Catalysts. *ChemCatChem* **2018**, *10*, 4292−4299.
(40) Binder, A. J.; Toops, T. J.; Parks, J. E. Copper−Cobalt−Cerium Ternary Oxide as an Additive to a Conventional Platinum-Group-Metal Catalyst for Automotive Exhaust Catalysis. *ChemCatChem* **2018**, *10*, 1263−1266.
(41) Wang, F.; Li, W.; Feng, X.; Liu, D.; Zhang, Y. Decoration of Pt on Cu/Co double-doped CeO2 nanospheres and their greatly enhanced catalytic activity. *Chem. Sci.* **2016**, *7*, 1867−1873.
(42) Cwele, T.; Mahadevaiah, N.; Singh, S.; Friedrich, H. B. Effect of Cu additives on the performance of a cobalt substituted ceria (Ce 0.90 Co 0.10 O 2−δ) catalyst in total and preferential CO oxidation. *Appl. Catal., B* **2016**, *182*, 1−14.
(43) Chen, S.; Zhao, S.; Xu, Z.; Liu, Z.; Zhu, R. Influence of pH on the catalytic performance of CuO−CoOx−CeO2 for CO oxidation. *RSC Adv.* **2015**, *5*, 61735−61741.
(44) Binder, A. J.; Toops, T. J.; Unocic, R. R.; Parks, J. E., 2nd; Dai, S. Low-Temperature CO Oxidation over a Ternary Oxide Catalyst with High Resistance to Hydrocarbon Inhibition. *Angew. Chem., Int. Ed. Engl.* **2015**, *54*, 13263−13267.
(45) Liu, Z.; Wu, Z.; Peng, X.; Binder, A.; Chai, S.; Dai, S. Origin of Active Oxygen in a Ternary CuOx/Co3O4−CeO2 Catalyst for CO Oxidation. *J. Phys. Chem. C* **2014**, *118*, 27870−27877.
(46) Liu, Z. G.; Chai, S. H.; Binder, A.; Li, Y. Y.; Ji, L. T.; Dai, S. Influence of calcination temperature on the structure and catalytic performance of CuOx-CoOy-CeO2 ternary mixed oxide for CO oxidation. *Appl. Catal., A* **2013**, *451*, 282−288.
(47) Chen, Y.; Liu, D.; Yang, L.; Meng, M.; Zhang, J.; Zheng, L.; Chu, S.; Hu, T. Ternary composite oxide catalysts CuO/Co3O4−CeO2 with wide temperature-window for the preferential oxidation of CO in H2-rich stream. *Chem. Eng. J.* **2013**, *234*, 88−98.
(48) Somekawa, S.; Hagiwara, T.; Fujii, K.; Kojima, M.; Shinoda, T.; Takanabe, K.; Domen, K. Mineralization of volatile organic compounds (VOCs) over the catalyst CuO-Co3O4-CeO2 and its applications in industrial odor control. *Appl. Catal., A* **2011**, *409*, 209−214.
(49) Park, H.; Lee, E. J.; Woo, H.; Yoon, D.; Kim, C. H.; Jung, C. H.; Lee, K. B.; Lee, K.-Y. Enhanced hydrothermal durability of Co3O4@CuO−CeO2 Core-Shell catalyst for carbon monoxide and propylene oxidation. *Appl. Surf. Sci.* **2022**, *606*, 154916.
(50) Zhang, J.; Wu, K.; Xiong, J. X.; Ren, Q. M.; Zhong, J. P.; Cai, H. D.; Huang, H. M.; Chen, P. R.; Wu, J. L.; Chen, L. M.; Fu, M. L.; Ye, D. Q. Static and dynamic quantification tracking of asymmetric oxygen vacancies in copper-ceria catalysts with superior catalytic activity. *Appl. Catal., B* **2022**, *316*, 121620.
(51) Yu, K.; Lou, L. L.; Liu, S.; Zhou, W. Asymmetric Oxygen Vacancies: the Intrinsic Redox Active Sites in Metal Oxide Catalysts. *Adv. Sci.* **2020**, *7*, 1901970.
(52) Qiu, Z. H.; Guo, X. L.; Mao, J. X.; Zhou, R. X. New Design and Construction of Abundant Active Surface Interfacial Copper Entities in CuxCe1-xO2 Nanorod Catalysts for CO-PROX. *J. Phys. Chem. C* **2021**, *125*, 9178−9189.
(53) Song, S.; Liang, J.; Xiao, W.; Gu, D. Dual-template synthesis of defect-rich mesoporous Co3O4 for low temperature CO oxidation. *Chin. Chem. Lett.* **2023**, *34*, 107777.
(54) Wang, Q.; Li, Z.; Banares, M. A.; Weng, L. T.; Gu, Q.; Price, J.; Han, W.; Yeung, K. L. A Novel Approach to High-Performance Aliovalent-Substituted Catalysts—2D Bimetallic MOF-Derived Ce-CuO_x Microsheets. *Small* **2019**, *15*, 1903525.
(55) Jia, A.-P.; Hu, G.-S.; Meng, L.; Xie, Y.-L.; Lu, J.-Q.; Luo, M.-F. CO oxidation over CuO/Ce1−xCuxO2−δ and Ce1−xCuxO2−δ catalysts: Synergetic effects and kinetic study. *J. Catal.* **2012**, *289*, 199−209.
(56) Guo, M.; Lu, J.; Wu, Y.; Wang, Y.; Luo, M. UV and visible Raman studies of oxygen vacancies in rare-earth-doped ceria. *Langmuir* **2011**, *27*, 3872−3877.
(57) Zou, Q.; Zhao, Y.; Jin, X.; Fang, J.; Li, D.; Li, K.; Lu, J.; Luo, Y. Ceria-nano supported copper oxide catalysts for CO preferential oxidation: Importance of oxygen species and metal-support interaction. *Appl. Surf. Sci.* **2019**, *494*, 1166−1176.
(58) Mao, Y.; Wang, P.; Li, L.; Chen, Z.; Wang, H.; Li, Y.; Zhan, S. Unravelling the Synergy between Oxygen Vacancies and Oxygen Substitution in BiO2-x for Efficient Molecular-Oxygen Activation. *Angew. Chem., Int. Ed. Engl.* **2020**, *59*, 3685−3690.
(59) Li, W.; Li, Y.; Zhang, D.; Lan, Y.; Guo, J. CuO-Co3O4@CeO2 as a heterogeneous catalyst for efficient degradation of 2,4-dichlorophenoxyacetic acid by peroxymonosulfate. *J. Hazard. Mater.* **2020**, *381*, 121209.
(60) Chen, A.; Yu, X.; Zhou, Y.; Miao, S.; Li, Y.; Kuld, S.; Sehested, J.; Liu, J.; Aoki, T.; Hong, S.; Camellone, M. F.; Fabris, S.; Ning, J.; Jin, C.; Yang, C.; Nefedov, A.; Wöll, C.; Wang, Y.; Shen, W. Structure of the catalytically active copper−ceria interfacial perimeter. *Nat. Catal.* **2019**, *2*, 334−341.

https://doi.org/10.1021/jacsau.4c01221
JACS Au 2025, 5, 975−989